

Characterization of Small Molecule Organic Solar Cells by Variable Light Intensity Measurements

Resumen Treball Final - Màster Interuniversitari UB-UPC d'Enginyeria en Energia - Convocatòria: Mayo 2013

Alumne: Luis Guillermo Gerling Sarabia; **Director:** Cristóbal Voz Sánchez

1. Introduction

The global energy system is based upon finite and polluting fossil sources that destabilize the global climate and cannot guarantee the energy needs of future generations. In addition, they are also unequally distributed: nowadays, 1.5 billion people lack electricity while half the population still relies on traditional biomass for cooking and heating [1]. Nevertheless, in 2011, modern renewable energy sources accounted for 8.2% of global final energy demand. Of all renewable sources, solar photovoltaics (PV) have the fastest development rate, resulting in 101 GW installed worldwide by the end of 2012, with roughly 87% of the market covered by crystalline silicon wafer technology and the rest by thin film technologies [2].

When compared to other renewable sources, PV offers distinctive advantages such as its resource abundance, scalability, grid-connection independence and its negligible operation and maintenance costs. Nonetheless, the Levelized Cost of Energy (LCOE) for PV technologies remains non-competitive with the electricity mix due to high capital costs (predominantly from wafer manufacturing and balance of system) and a great dependence on financing schemes.

During the last decade, solar cells based on solid-state organic photoactive materials have been investigated as an alternative to silicon technology. Organic Solar Cells (OSC) have been developed by using semiconducting organic materials which are capable of absorbing light and photo-generate charge carriers. Since they are thin film devices, their Energy Pay-Back Times (EPBT) could be less than one year and their life cycle CO₂ emissions could be below the electricity mix average [3] (Table 1.1).

Technology	η	EPBT (years)	eqCO ₂ /kWh
Mono Si	14%	2.7	81
Multi Si	13%	2.1	62
GaInP	26%	2.1	65
a-Si	7%	1.1	34
CdTe	9%	1.6	50
OSC Laboratory	10%	2.0	61
OSC Roll-to-roll	3%	1.4	35

Table 1.1 Energy pay-back times and life cycle CO₂ emissions of PV technologies.

However, in order to become cost-competitive with silicon solar cells, OSC technology still needs to *a)* reach conversion efficiencies above 10%, *b)* attain 10 years or more of operational stability, and *c)* be industrially feasible and allow for low manufacturing costs [4]. The maximum conversion efficiency achieved to date is 12%, while theoretical calculations suggest efficiencies up to 24% in single junction devices [5] (Figure 1.1).

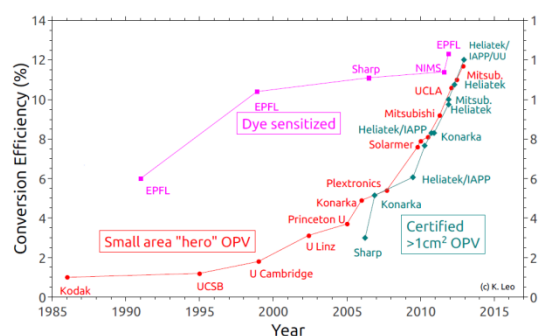


Figure 1.1 Conversion efficiencies of OSC [6].

Two types of semiconductor organic materials have been used to date: small molecule compounds (oligomers) and polymers (Figure 1.2), the former achieving record efficiencies and the latter leading commercialization efforts. Yet, small molecule OSC offer significant advantages over polymeric materials, such as synthesis flexibility to obtain the desired properties, repetitiveness and multilayering capabilities.

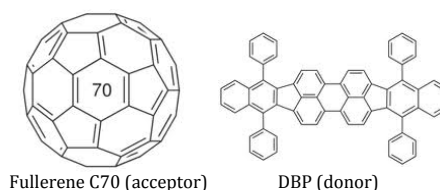


Figure 1.2 Oligomers used in small molecule organic solar cells.

The semiconductor effect in organic materials is explained via the sp^2 orbital hybridization in carbon double bonds ($-C=C-$), which have specific energy levels that permit electron transitions between them (Figure 1.3).

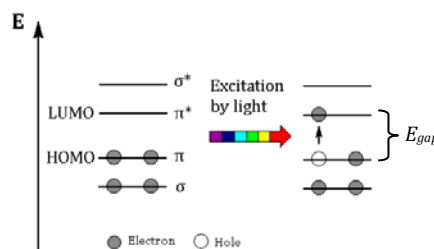


Figure 1.3 Energy levels of a molecular C=C bond before and after excitation.

In its unexcited state, electrons fill the low energy π orbital (known as the Highest Occupied Molecular Orbital - HOMO), while the high energy π^* orbital is unoccupied (known as the Lowest Unoccupied Molecular Orbital - LUMO). When one electron is excited, the HOMO-LUMO transition has an energy equivalent to the band gap energy (E_{gap}).

OSC work in donor-acceptor (D-A) heterojunctions (HJ). While the *p*-type material donates electrons through the D-A interface, the *n*-type material accepts them. When an organic

D-A system is excited by photons, Frenkel excitons (consisting of an electron-hole pair) are generated and then disassociate at the D-A interface so that each charge carrier (e and h) can travel to its corresponding electrode. Unfortunately, the mean distance excitons travel before they extinguish, L_{EX} , is very short (1-20 nm) according $L_{EX} = \sqrt{D_{EX}\tau_{EX}}$ (where D_{EX} is the exciton diffusivity). This limits the thickness of the D-A active layer to a few nm. Selection of materials with appropriate HOMO-LUMO levels also determines the maximum open circuit voltage (V_{OC}):

$$qV_{OC}^{max} = HOMO_D - LUMO_A - E_{e-h} \quad (1)$$

where E_{e-h} is the binding energy of the $e-h$ geminate pair after charge transfer [7]. Considering this, the conversion of light into electric current can be split into four different processes, each one with its own efficiency η_j (Figure 1.4) [8]:

- 1° Photon absorption and exciton generation, η_A .
- 2° Exciton diffusion to the D-A interface, η_{ED} .
- 3° Exciton charge transfer into electron-hole pairs, or, η_{CT} .
- 4° Charge transport and collection in the electrodes, η_{CC} .

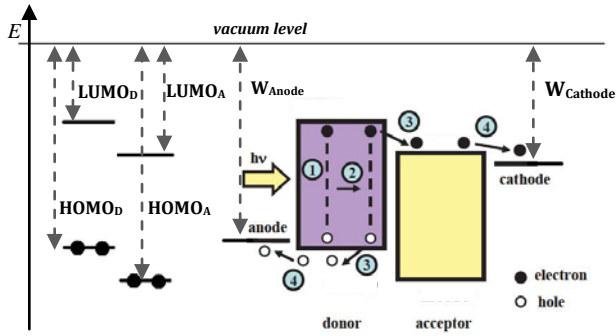


Figure 1.4 Elemental processes of an OSC: (1) exciton generation; (2) exciton diffusion; (3) exciton dissociation; (4) carriers transport and collection.

η_A is controlled by the solar absorption spectra of the active layers. In most cases, η_{ED} is the limiting process (usually <10%) due to low exciton diffusion length. It has been proven that optimal thickness of the active D-A layer is approximately equal to the L_{EX} of each constituent layer [9]. For the η_{CT} to be energetically favorable, the energy that binds the exciton, E_{EX} , needs to meet the condition $E_{EX} > HOMO_D - LUMO_A$. The carrier collection efficiency η_{CC} depends mainly on the built-in voltage V_{bi} (difference in work function of electrodes W_i).

The overall photon-to-electron efficiency, known as External Quantum Efficiency (EQE), defined as the ratio of photo-generated carriers collected by the electrodes to the number of the incidental photons, relates to the above efficiencies as:

$$EQE = \eta_A \times \eta_{ED} \times \eta_{CT} \times \eta_{CC} \quad (2)$$

The mean distance a charge carrier can drift under an electric field \vec{E} before suffering electron-hole recombination is:

$$l_{drift} = \mu_i \tau_i \vec{E} \quad (3)$$

The product $\mu_i \tau_i$, (mobility of the carrier by its life time) has to be maximized in order to attain a good cell performance. From adding the contributions of both charge carriers:

$$\mu \tau_{eff} = \mu_e \tau_e + \mu_h \tau_h \quad (4)$$

a global or effective $\mu \tau$ is obtained, describing the behavior of the OSC in a general way. Complex experimental methods and computational modeling can be used to determine the individual mobilities and lifetimes of the charge carriers, but they can be time and effort consuming. In this work, a simpler methodology based on Variable Illumination Measurements (VIM) has been used to achieve the following objectives:

- a) Analyze VIM data to determine the parameters that fit an equivalent solar cell circuit model.
- b) Determine an effective $\mu \tau$ for a series of organic solar cells with intrinsic (donor:acceptor ratio of 1:1) bulk HJ.
- c) Establish a link between the VIM parameters and cell degradation.

2. Experimental methods

Figure 2.1 describes a layer arrangement for the small molecule organic solar cells fabricated for this work. The D-A materials (p and n type) are the active layer of the device. The heterojunction morphology, known as bulk heterojunction, allows both materials to be thoroughly mixed together so that their interfaces are within a distance less than the exciton diffusion length. A transparent conductive oxide (Indium Tin Oxide, ITO) is used as anode due to its ability to transmit light and conduct charge, while aluminum is used as cathode. MoO_3 is used as a Hole Transport Layer (HTL) and BCP as an Electron Transport Layers (ETL), so as to promote the transfer of h and e into the anode and cathode, respectively.

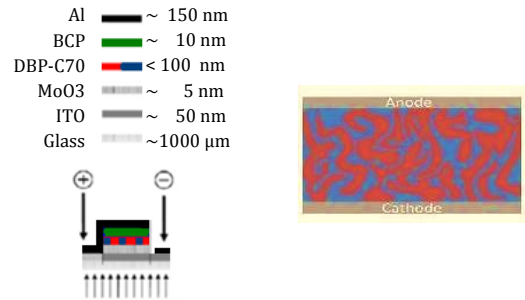


Figure 2.1 Solar cell architecture and bulk heterojunction morphology.

DBP has just recently been used as an electron donor, having unique properties such as a) HOMO level of 5.5 eV, resulting in a $V_{OC} > 0.9$ V [10], b) high absorption coefficient, and c) long L_{EX} (16±1 nm) and high hole mobility ($\sim 10^{-4}$ cm²/V·s) [11].

Fullerenes are widely used as acceptor material due to a) their complimentary absorption spectrum in relation to donor materials; b) its long L_{EX} (40±5 nm) [9] and high electron mobility (5×10^{-2} cm²/V·s) [12]. Table 2.1 shows some properties of the materials used. For the bulk HJ, a DBP and C70 were mixed in a ratio of 1:1 in order to approximately balance n and p charges and obtain a true intrinsic (i) layer.

Material	Initial T (°C)	Thickness(nm)/Dep Time(min)	HOMO-LUMO (eV)
ITO	/	45/NA	4.7-0
MoO ₃	/	3/≈5	5.4-2.3
DBP	≈250-300	10/≈30	5.5-3.5
C70	≈300-310	40/≈90	6.1-4.2
BCP	100-120	8/≈15	6.0-3.5
Al	/	150/≈70	4.1-0

Table 2.1 Material properties. Initial T is at 10⁻⁷ mbar.

The fabrication procedure consisted of *a)* substrate cleaning with ultrasonic acetone-isopropanol baths and UV-ozone treatment; *b)* deposition of MoO_3 ; *c)* deposition of organic materials; *d)* deposition of Al. A quartz crystal microbalance was used to measure the deposition rates (between 0.1 and 1 Å/s). All depositions were performed in high vacuum (10^{-7} mbar) inside a N_2 -atmosphere glove box. (Figure 2.2).



Figure 2.2 MBraun deposition chamber and N_2 -atmosphere glove box.

Optimal substrate temperature for the DBP layer was found to be 60°C , obtaining the crystalline structure that maximizes charge mobility of the charge carriers.

The aluminum contact evaporation is done through a shadow mask to fix the area of the cell resulting in 4 cells per substrate, each with an area of 0.075 cm^2 (Figure 2.3a). A thermal annealing treatment was done to re-crystallize the material and decrease shunts [13]. All characterization measurements were performed using a prototype that keeps the sample under N_2 atmosphere (Figure 2.3b).



Figure 2.3 a) Final 15x15 mm substrate with four cells, as defined by a shadow mask. b) Prototype for characterizing cells.

For the Power Conversion Efficiency (*PCE*) measurement, a standardized solar simulator (1.5 Air Mass, $1,000 \text{ W/m}^2$) was used, while a commercial measuring unit was utilized for EQE determination. Figure 2.4 shows the schematic of the VIM home-made system which measures and analyses the $J(V)$ curve under logarithmically varying illumination levels by using neutral grey filters.

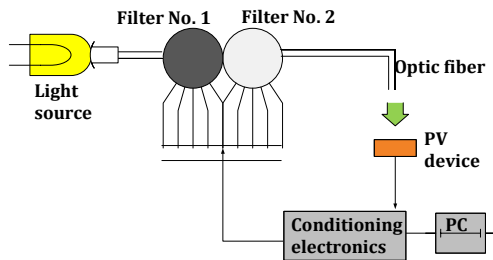


Figure 2.4 Variable Illumination Measurement system

3. Variable Intensity Measurements(VIM)

Figure 3.1 and Table 3.1 show the $J(V)$ curve and main performance parameters for a series of bulk HJ organic solar cells with different intrinsic layer thicknesses.

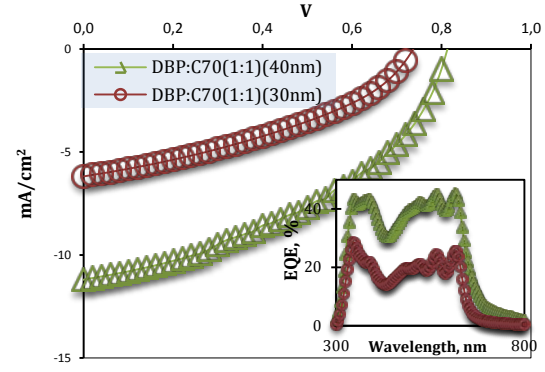


Figure 3.1 $J(V)$ curves for two different bulk thicknesses. Insert shows EQE.

	<i>PCE</i>	<i>FF</i>	P_{MAX} , mW/cm ²	J_{SC} , mA/cm ²	V_{OC} , V
DBP:C70(1:1)(40nm)	3.93%	43.3%	3.93	-11.20	0.81
DBP:C70(1:1)(30nm)	1.76%	39.0%	1.76	-6.19	0.73

Table 3.1 Main parameters for OSC with two different bulk thicknesses.

At first glance, the difference in conversion efficiencies could be attributed solely to the variation in the i-layer thickness and its absorption efficiency. Nevertheless, other quality factors such as layer imperfections and poor electrical properties could be in play. This becomes obvious when the $J(V)$ behavior is analyzed as an electric circuit (Figure 3.2):

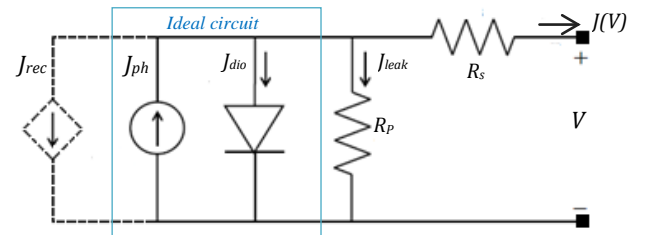


Figure 3.2 Generic equivalent circuit (without dashed segment) describing the real behavior of a solar cell.

The general equation that describes this circuit is:

$$J(V) = -J_{ph} + J_o \left(\exp \left(\frac{V - R_s J}{n V_T} \right) - 1 \right) + \frac{V - R_s J}{R_p} + J_{rec} \quad (5)$$

where J_{ph} is the photogenerated current, J_o is the reverse bias saturation current, n is the diode ideality factor, V is the voltage applied to the diode and V_T is the thermal voltage. The series and parallel resistances R_s and R_p dissipate power and reduce the efficiency of the cell. An extra loss term is J_{rec} , which is attributed to electron-hole recombination (current sink) and will be later added to the equivalent circuit in order to model the behavior of an intrinsic bulk HJ.

In order to estimate each of the terms in Eq. 5, the VIM method was applied to the aforementioned solar cell series. The main performance parameters (J_{SC} , V_{OC} , FF , $R_{OC} = (\partial V / \partial J)_{J=0}$ and $R_{SC} = (\partial V / \partial J)_{V=0}$ among others) were then plotted as a function of the short circuit current J_{SC} , avoiding the need to use calibrated illumination levels [14].

Figure 3.3 shows R_{OC} as a function of $\log(J_{SC})$, reaching the value of R_s at the highest illuminations. The main contribution for R_s comes from low conductivities of the bulk active layer (low carrier mobilities) and the electrodes (high sheet resistances).

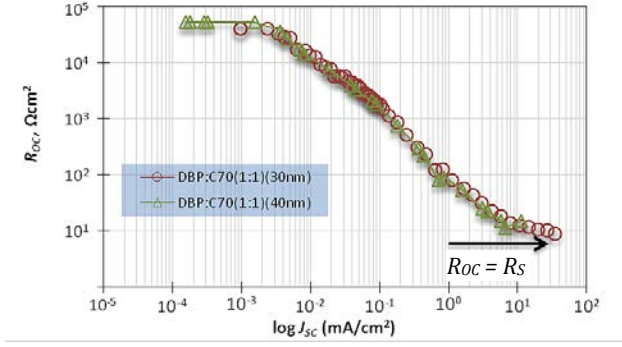


Figure 3.3 R_{oc} as a function of $\log(J_{sc})$.

Figure 3.4 shows R_{sc} as a function of $\log(J_{sc})$, reaching the value of R_p at the lowest illuminations. Often called shunt resistance, R_p is attributed in part to manufacturing defects such as shorts and pinholes that form conductive paths between the electrodes or that bypass the D-A interface.

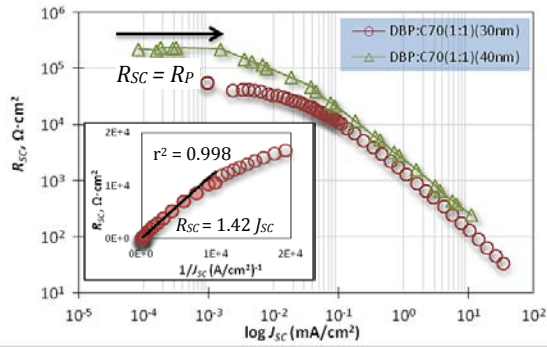


Figure 3.4 R_{sc} as a function of $\log(J_{sc})$. The insert depicts the best fit for the exponential regime.

Figure 3.5 shows V_{oc} as a function of $\log(J_{sc})$. On the medium illumination range a logarithmic fit of the curve can be made in order to obtain the characteristic diode terms n and I_0 .

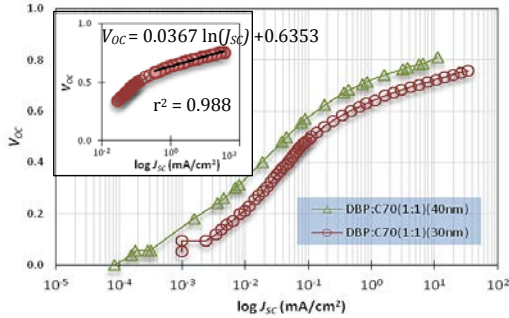


Figure 3.5 V_{oc} as a function of $\log(J_{sc})$. The insert depicts the best fit for the top exponential regime.

Table 3.2 summarizes the parameters obtained from the VIM:

	R_p , Ωcm^2	R_s , Ωcm^2	n	J_0 , mA/cm^2
DBP:C70(1:1)(40nm)	208,213	14	1.37	1.30×10^{-9}
DBP:C70(1:1)(30nm)	43,381	10	1.43	3.03×10^{-8}

Table 3.2 Values of the parameters obtained from the VIM analysis.

Since R_s is very similar for both devices and has a low value ($< 25 \Omega\text{cm}^2$), it slightly accounts for the drop in PCE . A low value of R_p (i.e. high current leakage) partially justifies the reduced PCE for the 30 nm i-layer.

In addition, the 30 nm i-layer has a saturation current J_0 (as obtained from the V_{oc} vs $\log(J_{sc})$ plot) one order of magnitude greater, decreasing further the value of $J(V)$.

Parting from the fact that R_{sc} is inversely proportional to J_{sc} (insert of Figure 3.4) over a wide range of illumination levels, the following expression can be applied:

$$R_{sc} = V_c \cdot J_{sc}^{-1} \quad (6)$$

where V_c is a constant factor referred as the collection voltage, which can be interpreted as that single point where all $1/R_{sc}$ slopes meet when extrapolated into the x axis Figure 3.6).

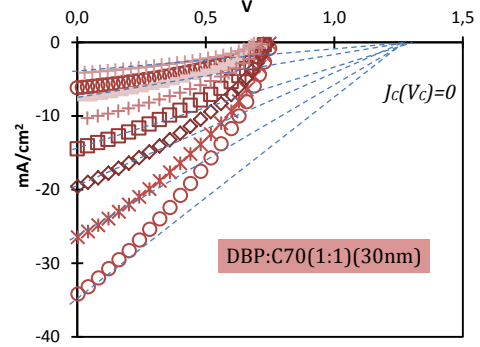


Figure 3.6 $J(V)$ curves for the OSC measured with the VIM. The collection voltage V_c is obtained by the x-axis intersection of the $1/R_{sc}$ slopes.

This collection voltage can be related to the recombination losses of the OSC by now adding the recombination current J_{rec} to the equivalent circuit, accounting for the recombination losses in the i-layer (bulk HJ) of the solar cell [14] [15]. A simple relationship between J_{rec} and R_{sc} may be obtained by differentiating Eq. 5 and evaluating it at short circuit conditions [16], so that:

$$\frac{1}{R_{sc}} \approx \left. \frac{\partial J_{rec}}{\partial V} \right|_{sc} = \frac{J_{sc}}{V_c} \quad (7)$$

Within this context, a lower V_c would mean higher recombination losses. A simple analytical model that relates V_c to the carrier transport quality of the organic intrinsic layer ($\mu\tau_{eff}$) can then be obtained by considering a few assumptions:

- Charge collection in the intrinsic bulk HJ is mainly a drift-driven process (no diffusion) [17].
- The electric field \vec{E} is constant across the whole length of the layer, as defined by $\vec{E} = (V_{bi} - V)/L$.
- The induced current is proportional to the sum of electrons and holes drift lengths, $l_c = l_e + l_h$ [17].

The validity of these assumptions is limited to small applied voltages, thin i-layers and low defect densities (or few traps for recombination) [14] [16], so that the recombination current becomes the sole factor that decreases the output current ($J = J_{ph} - J_{rec}$). With some algebra and by evaluating the derivative $\partial J_{rec} / \partial V|_{sc}$, a direct link between V_c and $\mu\tau_{eff}$ is established [16]:

$$R_{sc} = \left(\frac{2\mu\tau_{eff}V_{bi}}{L^2} - 1 \right) \frac{V_{bi}}{J_{sc}} = \frac{V_c}{J_{sc}} \quad (21)$$

After extracting the value of V_C from the experimental VIM data (Figure 3.4), the $\mu\tau_{eff}$ of each OSC is calculated (Table 3.3). The values are in close accordance with reported experimental data [18] [19].

	V_C , V	$\mu\tau_{eff}$, cm^2/V	I_C , nm	η_C	J_{reco} , mA/cm^2
DBP:C70(1:1)($L = 40nm$)	3.07	3.07×10^{-10}	173.5	88%	1.46
DBP:C70(1:1)($L = 30nm$)	1.42	3.56×10^{-11}	50.6	70%	2.60

Table 3.3 Values for the carrier collection process obtained from VIM analysis.

The results show some insight on the quality of the carrier transport process. A high $\mu\tau_{eff}$ can correlate to higher current extraction into the electrodes, indicating fewer losses by recombination (and higher *PCE*). Furthermore, collection lengths several times larger than the active i-layer result in high carrier collection efficiencies.

Finally, an insight on the causes of cell degradation can be obtained by applying the VIM methodology across a window of time. For the cell with 30 nm i-layer (1:1 DBP:C70), VIM measurements were done right after cell fabrication and then every 5 hours. Even though the cell was kept under N_2 atmosphere and it was only illuminated during data acquisition, the decrease in the conversion efficiency was substantial (59%). The largest contribution came from a J_{SC} drop of 54%, while *FF* dropped only by 7% and V_{OC} remained almost constant. Similar results were reported by [20].

Analysis of the characteristic resistances (Figure 3.7a) shows that, contrary to intuition, R_P increases with time. This indicates a lack of shunt formation during degradation. R_S increases slightly, somewhat explaining the decrease in *FF*. Figure 3.7b shows how $\mu\tau_{eff}$ also decreases with time, clearly representative of a loss in carrier mobility and/or lifetime.

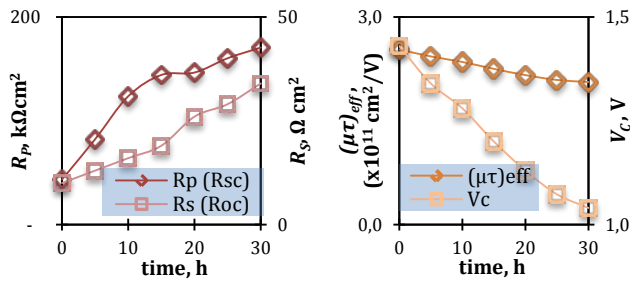


Figure 3.7 Resistance (a) and carrier collection (b) parameters for OSC with DBP:C70 (1:1, 30 nm), as obtained from VIM measurements across 30 hours.

4. Conclusions

It was the objective of this project to further understand the photon-to-electron conversion processes that occur within an OSC with the purpose of optimizing the different cell performance parameters.

Variable intensity measurements (VIM) were performed on a series of intrinsic bulk heterojunction cells with structure ITO/MoO₃/DBP:C70(1:1)/BCP/Al. Within the context of an equivalent electric circuit model, different parameters were obtained by analyzing the VIM data.

The R_S of the devices was found to have little influence on the *PCE*, with values below $15 \Omega cm^2$, while the lower R_P ($< 50 k\Omega cm^2$) was indicative of high current leakage that decreased the cell efficiency. VIM data was also used to quantify charge carrier transport quality by determining the effective mobility-lifetime product ($\mu\tau_{eff}$) as a function of the collection voltage V_C . A higher $\mu\tau_{eff}$ product correlated to higher J_{SC} , and consequently, higher charge collection efficiency.

In general, considering that the active materials selection was appropriate (high absorption, moderate exciton diffusion lengths), a poor *PCE* could be attributed to high current leakage and low $\mu\tau_{eff}$ s, resulting in very low fill factors (*FF* < 45%) and low charge collection efficiencies.

Finally, VIM data was analyzed during a time frame in search for signs of degradation. Although O₂-induced degradation was non-intentional, a clear deterioration of the *PCE* was observed, decreasing 59% in only 30 hours. The cause for deterioration is attributed to a failure of the N_2 -atmosphere packing of the measuring prototype, allowing O₂ to diffuse and deteriorate the active layer, resulting in a loss of J_{SC} and $\mu\tau_{eff}$.

In conclusion, all three objectives of this project were successfully achieved. The VIM methodology was proven to be consistent with the equivalent electric circuit model and its underlying assumptions. In general, a deeper understanding of the organic solar cell operation mechanisms was accomplished. As for future work, the DBP:C70 ratio needs to be optimized, VIM experiments should be done using the same wide-range illumination and additional measurements have to be done to determine the degradation effects on the device.

5. References

- [1] U. N. D. Programme, Human Development Report, 2011.
- [2] REN21, Renewables 2012 Global Status Report, 2012.
- [3] N. Espinosa, R. García-Valverde, A. Urbina & F. Krebs, Sol. Energy Mat. Sol. Cells, **95**, 1293-1302, 2011.
- [4] F. Krebs & al., Materials Today, **15**, núm. 1-2, 36-49, 2012.
- [5] R. A. J. Janssen & J. Nelson, Adv. Mater., **25**, 1847-1858, 2013.
- [6] I. f. A. Photophysik, May 2013. Available: <http://orgworld.de>.
- [7] B. Rand & D. Burk, Phys. Rev. B, **75**, 115327, 2007.
- [8] I. Bruder, PhD Thesis, Stuttgart University, **12**, 2010.
- [9] P. P. Neumans, & S. Forrest, J. Appl. Phys., **93**, 3693, 2003.
- [10] D. Fujishima, H. Kanno, T. Kinoshita & K. Shibata, Sol. Energy Mater. Sol. Cells, **93**, 1029, 2009.
- [11] X. Xiao, J. Zimmerman, B. Lassiter, K. Bergemann & S. Forrest, Appl. Phys. Lett., **102**, 073302, 2013.
- [12] H. Hoppe & N. S. Sariciftci, J. Mater. Res., **19**, 1924, 2004.
- [13] M. Vogel, J. Strotmann, B. Johnev & K. Fostiropoulos, Thin Solid Films, **511**, 367, 2006.
- [14] J. Merten, C. Voz, A. Muñoz, J. Asensi & J. Andreu, Sol. Energy mater. Sol. Cells, **57**, 153, 1999.
- [15] C. Hof, A. Shah, J. Non-Cryst. Solids, **266**, 1114, 2000.
- [16] C. Voz, J. Puigdollers, J. Asensi, S. Galindo, S. Cheylan, R. Pacios, P. Ortega & R. Alcubilla, Org. Electronics, **14**, 1643, 2013.
- [17] R. Crandall, J. Appl. Phys., **54**, 7176, 1983.
- [18] R. Street & M. Schoendorf, Phys. Rev B, **81**, 205307, 2010.
- [19] C. Deibel, Phys. Status Solidi, **206**, 2731, 2009.
- [20] A. Seemann, T. Sauermann, C. Lungenschmied, O. Armbruster, H. Egelhaaf & J. Hauch, Sol. Energy, **85**, 1238, 2011.